



The Birth of a Jet-driven Twin CME and Its Deflection from Remote Magnetic Fields

Yadan Duan¹, Yuandeng Shen^{2,3} , Hechao Chen^{2,3,4} , and Hongfei Liang¹¹ Yunnan Normal University, Department of Physics, Kunming 650500, Yunnan, People's Republic of China; ydshen@ynao.ac.cn, lhf@ynao.ac.cn² Yunnan Observatories, Chinese Academy of Sciences, Kunming, 650216, People's Republic of China³ Center for Astronomical Mega-Science, Chinese Academy of Sciences, Beijing, 100012, People's Republic of China⁴ University of Chinese Academy of Sciences, 19A Yuquan Road, Shijingshan District, Beijing 100049, People's Republic of China

Received 2019 May 6; revised 2019 July 14; accepted 2019 July 15; published 2019 August 21

Abstract

We report the formation of a complicated coronal mass ejection (CME) on 2015 August 23 by using the high temporal and high spatial resolution multi-wavelength observations taken by the *Solar Dynamic Observatory* and the *Solar and Heliospheric Observatory*. The CME exhibited both jetlike and bubble-like components simultaneously, and therefore, we call it a twin CME. Detailed imaging and kinematic analysis results indicate that the twin CME was evolved from the eruption of a mini-filament-driven blowout jet at the eastern edge of an equatorial coronal hole, in which the activation of the mini-filament was tightly associated with the continuous flux cancellation and quasi-periodic jetlike activities in the filament channel. Due to the magnetic reconnection between the filament and the ambient open field lines, the filament broke partially at the northern part and resulted in an intriguing blowout jet in the southern direction. It is interesting that the ejecting jet was deflected by a group of remote open field lines, which resulted in the significant direction change of the jet from southward to eastward. Based on the close temporal and spatial relationships among the jet, filament eruption, and the twin CME, we conclude that the jetlike CME should be the coronal extension of the jet plasma, while the bubble-like one should have originated from the eruption of the mini-filament confined by the closed magnetic fields at the jet base.

Key words: Sun: activity – Sun: coronal mass ejections (CMEs) – Sun: filaments, prominences

Supporting material: animations

1. Introduction

Solar eruptions are eruptive transient magnetic activities in the solar corona, in which magnetic energy can be released to heat and eject the magnetized plasma. Such ejection of plasma from lower to upper layers in the solar atmosphere can be divided into two classes (Filippov & Den 2018). The first class of solar eruptions is the most spectacular large-scale magnetized plasma eruption, i.e., coronal mass ejections (CMEs). Typically, they often occur accompanying solar flares and demonstrate as bubble-like or loop-like shape in the outer corona, and they are generally considered to be driven by magnetic structures, such as magnetic flux ropes and filaments (e.g., Lin & Forbes 2000; Liu et al. 2010a; Shen et al. 2011c, 2012a, 2018b; Yang & Chen 2019). The projection speed of CMEs ranges from ~ 20 to 2000 km s^{-1} , and their average speeds increase from 300 km s^{-1} near the solar minimum to 500 km s^{-1} near the solar maximum (Yashiro et al. 2004). Generally, the eruption direction of CMEs is often along the radial direction from the solar center propagating into the interplanetary space. However, some CMEs also show direction deviation with respect to the solar radial direction (MacQueen et al. 1986; Jiang et al. 2007, 2008). The direction deviation of a CME might take place in both the latitude and longitude in the interplanetary (Byrne et al. 2010; Liu et al. 2010b; Davies et al. 2013; Isavnin et al. 2013; Zhou & Feng 2013). Gopalswamy et al. (2004, 2009), given that corona holes are responsible for the deflection of CMEs away from the Sun–Earth line. Kilpua et al. (2009) suggest that during the solar minimum period, the low detection rate of interplanetary CMEs at ecliptic plane may be increased if CMEs are guided toward the equator from their high-latitude source regions by the magnetic fields in the polar coronal holes.

Yang et al. (2018) reported the nearly 90° direction change of a CME compare to the initial eruption direction due to the deflection of the open coronal hole magnetic fields. Shen et al. (2011a) and Gui et al. (2011) considered that the CME deflection is related to gradients in the magnetic energy density of the background solar corona. Deflection effects of CMEs can also caused by nearby strong magnetic structures (e.g., Jiang et al. 2007; Bi et al. 2011, 2013). For space weather forecasting, the better we understand the deflected trajectory of a CME through the low corona to the heliosphere, the better we can predict the its near-Earth effects (Kay et al. 2013).

The second class of solar eruption is in the form of short-term, thin, and collimated jets from lower layers of the solar atmosphere. Solar jets are ubiquitous and can be observed in active regions, quiet-Sun regions, and corona holes (Shibata et al. 1992, 1994; Yang et al. 2011; Chen et al. 2012, 2017; Li & Zhang 2013; Tian et al. 2014). According to different observing wavelengths, solar jets can be divided into $H\alpha$ surges, extreme ultraviolet (EUV) jets, and X-ray jets (Roy 1973; Canfield et al. 1996; Chae et al. 1999; Zhang et al. 2000; Liu et al. 2009; Zhang & Ji 2014; Li et al. 2018; Tian et al. 2018a; Yang & Zhang 2018; Hou et al. 2019). Yokoyama & Shibata (1995, 1996) performed two-dimensional magnetohydrodynamics (MHD) simulations for solar X-ray jets by using two magnetic initial configurations to generate anemone and two-sided loop jets. The ejection of the two types of jets are all caused by the magnetic reconnection between emerging and nearby coronal fields. Magnetic reconnection between emerging bipoles and their ambient open magnetic field lines is considered to be the cause of most collimated solar jets (e.g., Shibata et al. 1994; Liu & Kurokawa 2004; Shen et al. 2011b). When emerging fluxes reconnect with overlying horizontal magnetic fields, two-sided loop jets are produced

(Yokoyama & Shibata 1995; Kundu et al. 1998; Jiang et al. 2013). Besides flux emergence, many observations have indicated that flux cancellation is also important for triggering solar jets (e.g., Shen et al. 2012b, 2017; Yang et al. 2012b; Adams et al. 2014; Panesar et al. 2016; Joshi et al. 2017). Shibata et al. (1992) found that the typical size of X-ray jets ranges from 5×10^3 to 4×10^5 km, their velocity is in the range of $30\text{--}300 \text{ km s}^{-1}$, and the corresponding kinetic energy is in the range of $10^{25} \sim 10^{28}$ erg. Interestingly, solar jets sometimes can directly or indirectly launch large-scale coronal waves (e.g., Shen et al. 2018a, 2018c, 2018d) and CMEs (e.g., Wang et al. 1998; Wang & Sheeley 2002; Liu et al. 2005; Jiang et al. 2008; Liu 2008; Shen et al. 2012b). For the generation of two-sided loop jets, recent high-resolution observations indicated that other mechanisms can also trigger them (Tian et al. 2017; Huang et al. 2018; Zheng et al. 2018; Sterling et al. 2019). In particular, Tian et al. (2018b) found that two-sided loop jets in the filament channel can result in the loss of equilibrium and eruption of large-scale filaments.

Moore et al. (2010) proposed that there is a dichotomy of solar jets; they reclassified solar anemone jets as standard jets and blowout jets. They found about that two thirds of solar anemone jets are standard jets, while the rest of the one third are blowout jets. With high-resolution observations, more and more studies confirmed the finding of blowout jets (Shen et al. 2012b; Hong et al. 2013, 2016, 2017; Adams et al. 2014; Lee et al. 2015; Li et al. 2015, 2017a, 2017b, 2018; Zhang & Zhang 2017; Zhu et al. 2017; Miao et al. 2018, 2019; Yang & Zhang 2018; Li & Yang 2019). Compare with standard jets, the blowout jets are characterized by an initially narrow spire that later broadens. An initial compact brightening spreads to the whole jet base; the existence (or appearance) of a cool component ($T \sim 10^5$ K) visible in EUV 304 Å images (Moore et al. 2010; Sterling et al. 2015). Several studies have found that the blowout jets are often associated with the eruptive mini-filament (e.g., Shen et al. 2012b, 2017; Yang et al. 2012a; Adams et al. 2014; Sterling et al. 2016, 2015). Sterling et al. (2015) reported 20 randomly selected X-ray jets where all 20 jets originated from mini-filament eruptions, and they further suggested that standard jets and blowout jets are basically the same phenomenon whose morphology depends on the specific situation of mini-filament eruption. Shen et al. (2011b) and Hong et al. (2013) indicated that some blowout jets display untwisting motion, which may result from the erupting mini-filaments or strongly twisted structures in the jet base. These observations suggested that mini-filament eruptions play an important role in the generation of solar jets. The untwisting motion and the origin of the cool component in the jet base thus have been well explained because of the inclusion of the mini-filament (Shen et al. 2011b, 2012b, 2017).

Previous observations have suggested that small-scale solar jets have significant similarities with larger-scale solar eruptions. Investigating and revealing their similarities and differences is of great significance in order to explain multi-scale solar eruption phenomena. In particular, Shen et al. (2012b), for the first time, reported that a pair of simultaneous CMEs that are directly evolved from a single coronal blowout jet, in which one is in a jetlike shape and the other is in a bubble-like shape. Indeed, it is well documented in the literature that EUV jets present a white-light counterpart observed with coronagraphs (Nisticò et al. 2009, 2010; Paraschiv et al. 2010; Feng et al. 2012) in the form a narrow

emission, which is different from the standard CME picture. This study provided a new thought for understanding the generation of large-scale CMEs from small-scale jet activities. Afterward, many similar events were reported (Alzate & Morgan 2016; Miao et al. 2018, 2019; Solanki et al. 2019), and they are well explained by the model presented in Shen et al. (2012b). In addition, Archontis & Hood (2013) performed a three-dimensional numerical simulation that reproduced the observations presented in Shen et al. (2012b), but they did not investigate the CMEs in the outer corona. Observing and studying such kind of events is helpful for understanding the coupling phenomenon of multi-scale eruptive solar activities. However, similar studies are still very scarce.

In this paper, we report a mini-filament-driven blowout jet in the low corona, which unambiguously resulted in a twin CME in the outer corona. Compared with previous studies, the advantage of this event is that eruption source region is located at E40°N6° and suffers from a less projection effect. Thus, more accurate observational information during the initiation stage of the CME can be better obtained. More interestingly, we notice that the jet underwent an obvious deflection process due to its interaction with a group of remote open coronal loops, which resulted in the ejecting direction of the jet (or CME) changed significantly. These observations provide new clues for our understanding of coronal jets and CMEs. The paper is structured as follows: Section 2 describes instruments and data, Section 3 describes observations and results, and a summary and discussion are presented in Section 4.

2. Observation and Data Analysis

The blowout jet occurred on 2015 August 23 in a quiet-Sun region (E40°N6°) near the eastern edge of an equatorial coronal hole. To study the generation of the jet and the associated CMEs in detail, we use observations mainly from the Atmospheric Imaging Assembly (AIA; Lemen et al. 2012) on board the *Solar Dynamics Observatory* (SDO; Pesnell et al. 2012). AIA takes images of the Sun with seven EUV, two UV, and one visible wavelength channels. The spatial resolution of the AIA images is of 0''.6, and the cadences for the EUV, UV, and visible channels are 12 s, 24 s, and 1 hr, respectively. The eruption can be observed at all AIA EUV channels, and we mainly use the 171, 304, 94, and 211 Å images. The Helioseismic Magnetic Imager (HMI; Scherrer et al. 2012) line-of-sight (LOS) magnetograms are used to investigate the corresponding photospheric magnetic field evolution, which has a cadence of 720 s and a pixel size of 0''.6. The white-light observations taken by the Large Angle and Spectrometric Coronagraph (LASCO; Brueckner et al. 1995) are used to study the CME evolutions. Meanwhile, H α images taken by the Global Oscillation Network Group (GONG; Harvey et al. 2011; see Figures 1(a)–(c)) are also used and have a pixel size of 1'' and a cadence of 1 minute. To rule out the possibility that twin CME originate from the solar backside, we also applied observations from the Extreme Ultraviolet Imager (EUVI; Wuelser et al. 2004) of the Sun Earth Connection Coronal and Heliospheric Investigation (SECCHI; Howard et al. 2008) on board the *Solar Terrestrial Relations Observatory*-Ahead (STEREO-A; Kaiser et al. 2008). We also utilize the Potential Field Source Surface (PFSS; Schrijver & De Rosa 2003) model to investigate the primary three-dimensional magnetic topology around the eruption source region. In addition, radio observations provided by the Radio and Plasma WAVE Experiment

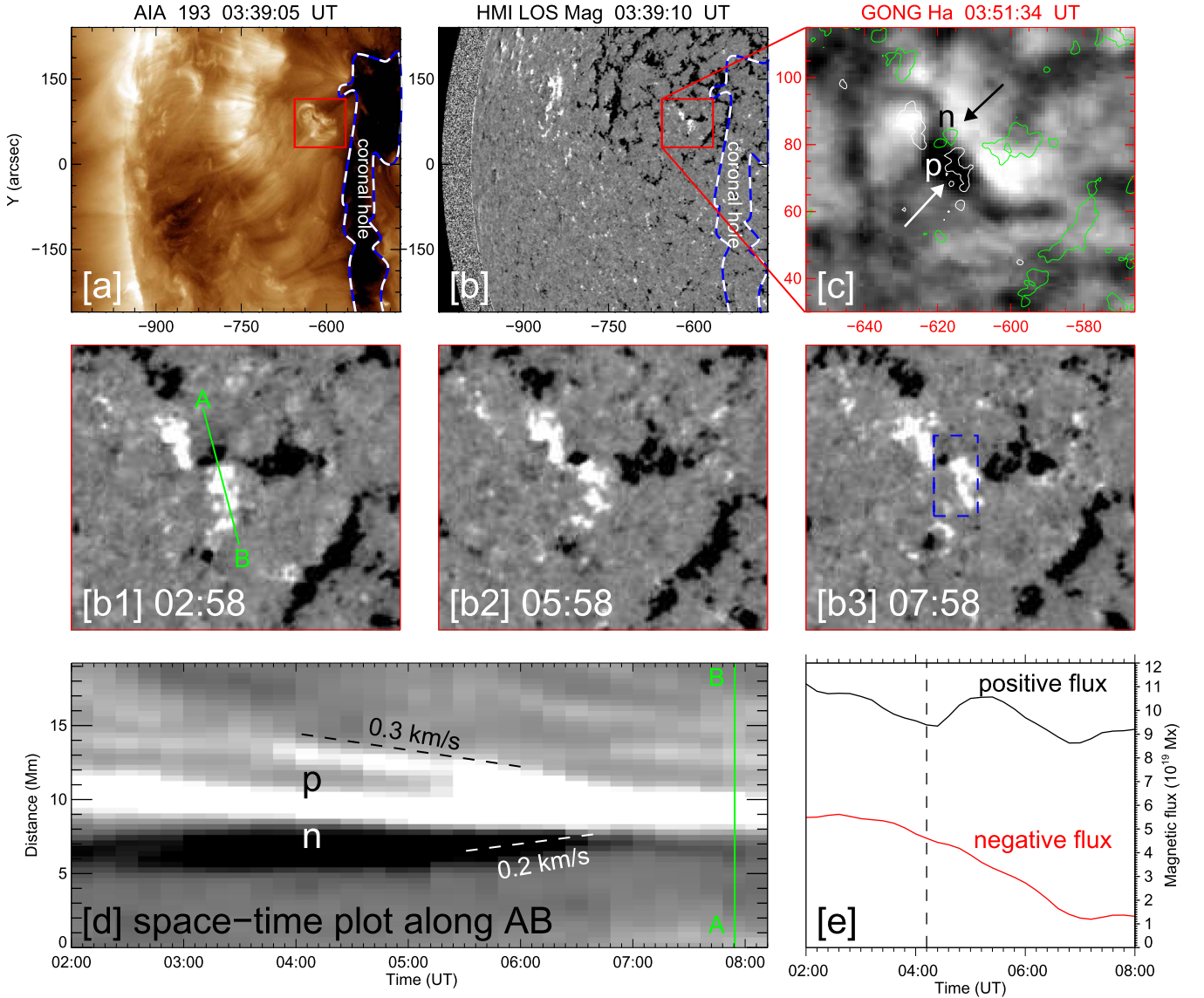


Figure 1. Panels (a) and (b): the magnetic field environment of the event, the white-blue dashed line outlines the boundary of the equatorial coronal hole. The red boxes denote the FOV of panels (b1)–(b3) and (c). Panel (c): a GONG H α image overlaid with the photospheric magnetic fields, in which positive and negative fields are plotted in white and green contours, and the corresponding scale levels are ± 50 G, respectively. Panels (b1)–(b3): time sequence HMI LOS magnetograms show the flux convergence and cancellation, in which the white (black) patches are positive (negative) magnetic polarities. Panel (d): the time–distance plot along the green line A–B in panel (b1). Panel (e): the positive (black) and negative (red) flux variations in time are indicated in the blue dashed box in panel (b3) from 02:00 UT to 08:00 UT, and the black dashed line indicates the start time of the mini-filament eruption.

(WAVES; Bougeret et al. 1995) on board the *Wind* spacecraft are utilized to detect the associated interplanetary radio signals. Accordingly, WAVES provide two radio detectors: RAD1 (0.02–1.04 MHz) and RAD2 (1.075–13.825 MHz). To compensate for solar rotation, all the images taken at different times are differentially rotated to a reference time of 04:15 UT.

3. Results

3.1. Activation and Initiation of the Mini-filament

On 2015 August 23, a mini-filament (with a length of ≈ 30 Mm) resided in a mixed-polarity quiet-Sun region at the eastern edge of an equatorial coronal hole, and it can be well distinguished in the H α image (Figures 1(a)–(c)). In order to understand the activation and eruption of the mini-filament, we investigate the evolution of the photospheric magnetic field within the eruption source region. HMI LOS magnetograms

show that continuous flux convergence and cancellation took place near the polarity inversion line of a pair of opposite polarities. The converging motion of the opposite polarities was along the path, as shown by the green line in Figure 1(b1). One can see that the area of the black negative polarity became smaller and smaller from 02:58 UT to 07:58 UT (see Figures 1(b1)–(b3)). The temporal variations of the positive and negative polarities are also showed as a time–distance plot in Figure 1(d), which better shows the convergence and cancellation processes of the opposite polarities. Here, the time–distance diagram is obtained by composing the time sequence of the intensity profiles along A–B. In addition, the converging speeds of the positive and negative polarities were also measured to be about 0.3 and 0.2 km s $^{-1}$, respectively. We also calculate the flux variations in the box region, as shown in Figure 1(b3), and the result is shown in Figure 1(e). It is clear that the unsigned negative flux decreased from 5.0 to 1.0×10^{19} Mx, while the positive flux

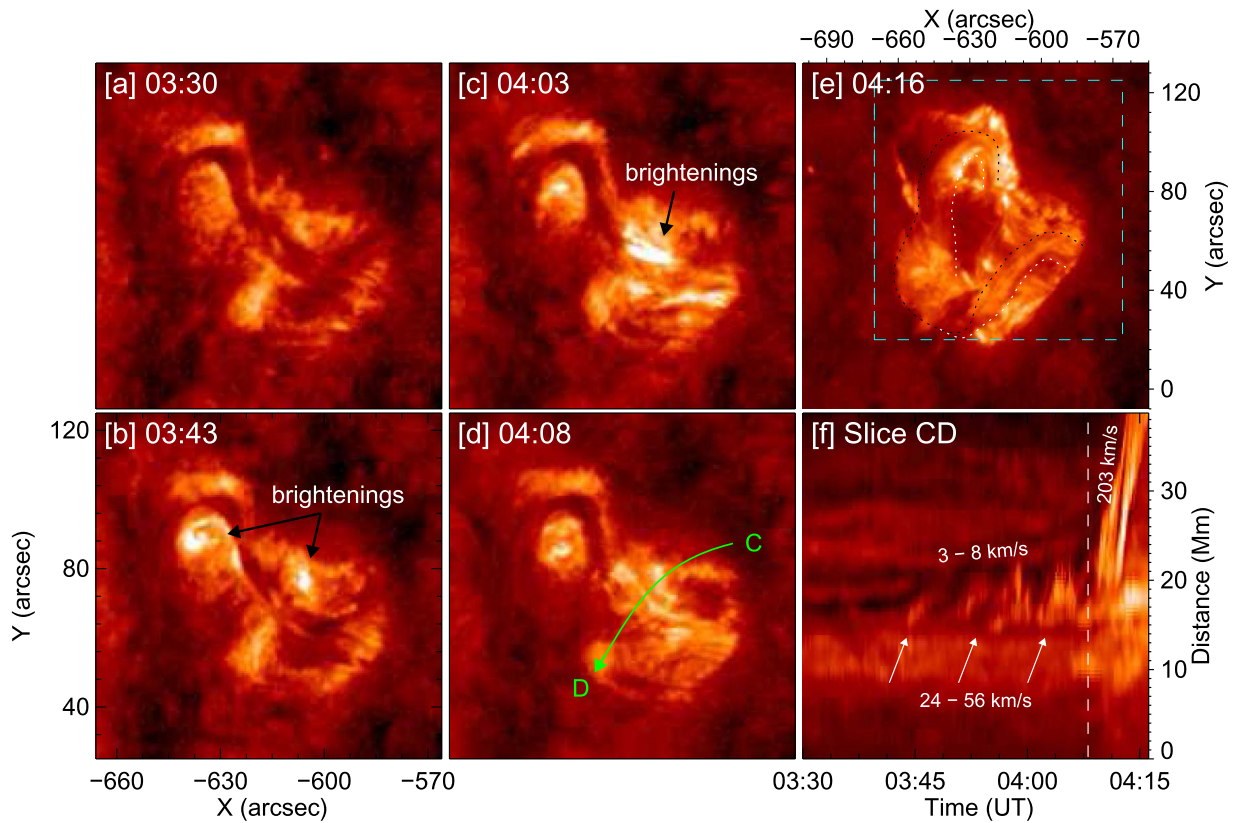


Figure 2. Panels (a)–(e): the activation and eruption of the filament observed in AIA 304 Å images. The black and white dashed lines in panel (e) outline the twisted filament, and the cyan dashed box indicates the FOV of panels (a)–(d). The time–distance plot along the green curve arrow C–D in panel (d) is shown in panel (f). The white arrows in panel (f) denote intermittent jetlike features, and the vertical white dashed line indicates the start time of the mini-filament eruption.

decreased from 11.0 to 9.0×10^{19} Mx. This flux changing pattern clearly suggests flux cancellation between the positive and negative fluxes. In addition, the positive flux also showed a small bump during 04:10 UT–06:50 UT, which indicates the emergence of the positive polarity. The start time of the positive flux’s increase was coincident with the start time of the filament eruption.

The activation and initiation of the mini-filament eruption are shown in Figure 2 using the AIA 304 Å images. The filament showed an inverse-S shape at about 03:30 UT (see panel (a)). A few minutes before the eruption, weak brightenings were observed at the middle section of the filament, which lasted for a few minutes and became more and more pronounced (see panels (b)–(d)). During this stage, intermittent jetlike features were observed below the filament. After the brightenings and intermittent jetlike activities, the filament started to erupt at about 04:10 UT, then it rapidly erupted to the southeastern direction accompanied by a lateral rolling motion. To further demonstrate the dynamical evolution of the filament, a time–distance plot is made along the green curve C–D in panel (d). One can see that before the filament got into its main eruption phase, intermittent jetlike features took place below the filament body, and they showed a quasi-periodic ejection behavior. The average time interval between neighboring jetlike features was about 335 s; they lasted for about 25 minutes from 03:45 UT to 04:10 UT with a speed in the range of about $24\text{--}56\text{ km s}^{-1}$. Note that before the violent eruption of the filament, it underwent a slow rising phase at a projection speed of $3\text{--}8\text{ km s}^{-1}$ (see panel (f)).

Based on the investigation of the variation of the magnetic flux and the eruption behavior of the filament described above, it is

clear that the filament activation and initiation were associated with the flux cancellation and emergence in the photosphere. Before the violent eruption stage of the mini-filament, the continuous flux cancellation caused the intermittent jetlike features and brightenings below the filament that also showed a slow rising phase of about 25 minutes. At about 04:10 UT, the sudden emergence of the positive flux accelerated its cancellation to the negative flux; this may directly destroy the quasi-equilibrium state of the filament, which therefore resulted in its violent eruption. It should be pointed out that the violent eruption of the filament could also be caused by kink instability after its activation, since strong rolling motion is observed in the erupting filament (Shen et al. 2012a).

3.2. Formation of the Blowout Jet

The erupting mini-filament transformed into a blowout jet via its magnetic reconnection with the ambient open magnetic fields. In Figure 3 and its animation, the AIA multi-wavelengths observations clearly captured the magnetic reconnection process. To better illustrate the reconfiguration of the magnetic fields during this stage, we plot the changes of different loops in Figure 3. As shown in panel (a), the loop structures involved in the reconnection are denoted by arrows “L1,” “L2,” and “L3,” respectively. Here, L1 refers to the pre-existing ambient open fields before the reconnection; L2 and L3 refer to the newly formed loops after the reconnection. By overlaying the axis of the erupting filament and the HMI LOS magnetogram on the AIA 211 Å running-difference image at 04:26 UT (the running-difference image is obtained by subtracting the current image

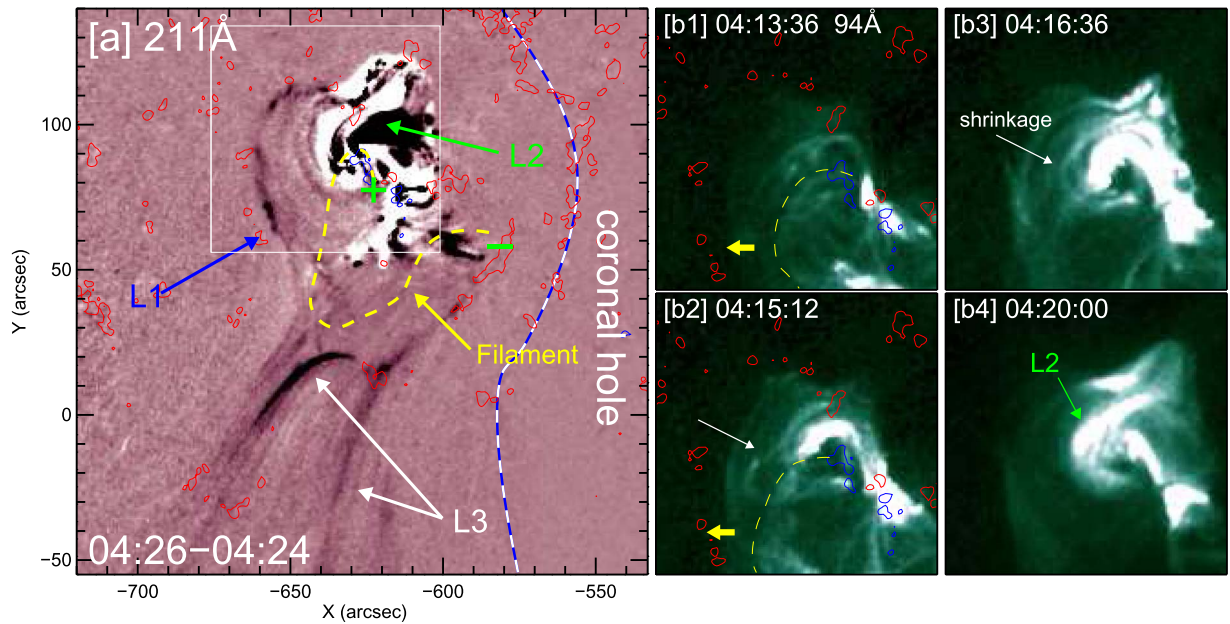


Figure 3. Panel (a): AIA 211 Å running-difference image demonstrates the magnetic configuration, in which the yellow dashed line denotes of the filament. The green “±” symbols indicate the two feet of the filament. The blue arrow points to the background open field lines (L1). The green (L2) and white (L3) arrows show some newly formed loops. The white-blue dashed line marks the eastern outline of the nearby coronal hole. The white box denotes the FOV of (b1)–(b4). Panels (b1)–(b4): time sequence of AIA 94 Å images show the formation process of L2. The yellow arrows indicate the moving direction of the filament, which is indicated by the yellow dashed line. The green arrow denotes the shrinkage L2. The red and blue contours in panels (a), (b1), and (b2) are positive and negative magnetic fields of the HMI LOS magnetogram scaled at ± 50 G, respectively. An animation of 211 and 94 Å is available. The animation covers 04:10–04:30 UT with a 12 s cadence. The animation duration is 3 s.

(An animation of this figure is available.)

from the previous one that taken at 04:24 UT), one can easily identify that the northern and the southern feet of the filament were rooted in negative and positive magnetic regions, respectively. Note that the ambient open field lines (L1) were rooted in a positive magnetic region. Therefore, it is clear that the directions of the magnetic fields of L1 and the axial field of the erupting filament were opposite, which is in favor of the occurrence of magnetic reconnection. Due to the interaction of the erupting filament with L1, the magnetic reconnection between them resulted in the generation of two groups of newly formed magnetic field lines, i.e., L2 and L3. L2 was observed as lower closed post-flare-loops, while L3 was shown as open field lines with the erupting filament mass along it (i.e., the jet). Moreover, the AIA 94 Å images in panels (b1)–(b4) further displayed the rapid formation and shrinkage process of L2 (see the animation of Figure 3). As indicated by the yellow dashed curves, the erupting filament approached the ambient open field lines and triggered the magnetic reconnection between them at about 04:13 UT (see panels (b1) and (b2)). Then, a group of closed and bright high-temperature loops formed about one minute later (see panel (b3)), and it quickly shrunk down at about 04:20 UT. These remarkable topological changes well evidence the reconnection process that break the erupting filament and led to the formation of the blowout jet.

3.3. Deflection of the Blowout Jet and the Formation of the CMEs

In this section, we focus on how the blowout jet finally developed into a twin CME in the outer corona. The multi-wavelength images in Figures 4(a1)–(a4) show that the hot plasma component of the jet is not obvious in high-temperature channels (i.e., 94 and 335 channels). The time sequence AIA

171 Å running-difference images in the middle row of Figure 4 show the ejection process of the blowout jet. As the filament reconnected with the ambient open fields, a spire structure formed ahead a U-shaped closed magnetic structure (see Figure 4(b1)). With the persistent break of the eastern leg of the U-shaped structure, the mass released from the closed filament became more conspicuous. Afterward, filament plasma is ejected along the newly formed open field lines (L3) and therefore formed the blowout jet. Untwisting signals of the filament can also be discerned in the formation course of the blowout jet, which consistent with previous observations (Shen et al. 2011b, 2012b, 2019; see the animation of Figure 4). Because of the releasing of the filament twist due to the magnetic reconnection between the filament and the ambient open fields, the blowout jet showed a wide spire and ejected outward with an obvious clockwise unwinding motion when looking above the jet axis.

It is striking that the ejection of the blowout jet was almost in the southern direction at the beginning, then it changed to southeastern direction at around 04:24 UT (see Figures 4(b3), (b4), and (c)). A time–distance plot along the line E–F as shown in Figure 4(c) is plotted in Figure 4(d), from which one can find that the jet body underwent an expansion and contraction motions during 04:22 UT–04:33 UT. The speeds of the expansion and contraction motion of the jet body along the line E–F were about 177 km s^{-1} and $61\text{--}280 \text{ km s}^{-1}$, respectively.

The three-dimensional coronal magnetic field is extrapolated based on the photospheric magnetic field using the PFSS (Schrijver & De Rosa 2003) to investigate the physical reason that caused the direction change of the blowout jet (see Figure 5). The result of the PFSS model can be obtained by using a software package in SolarSoftWare, which is based on

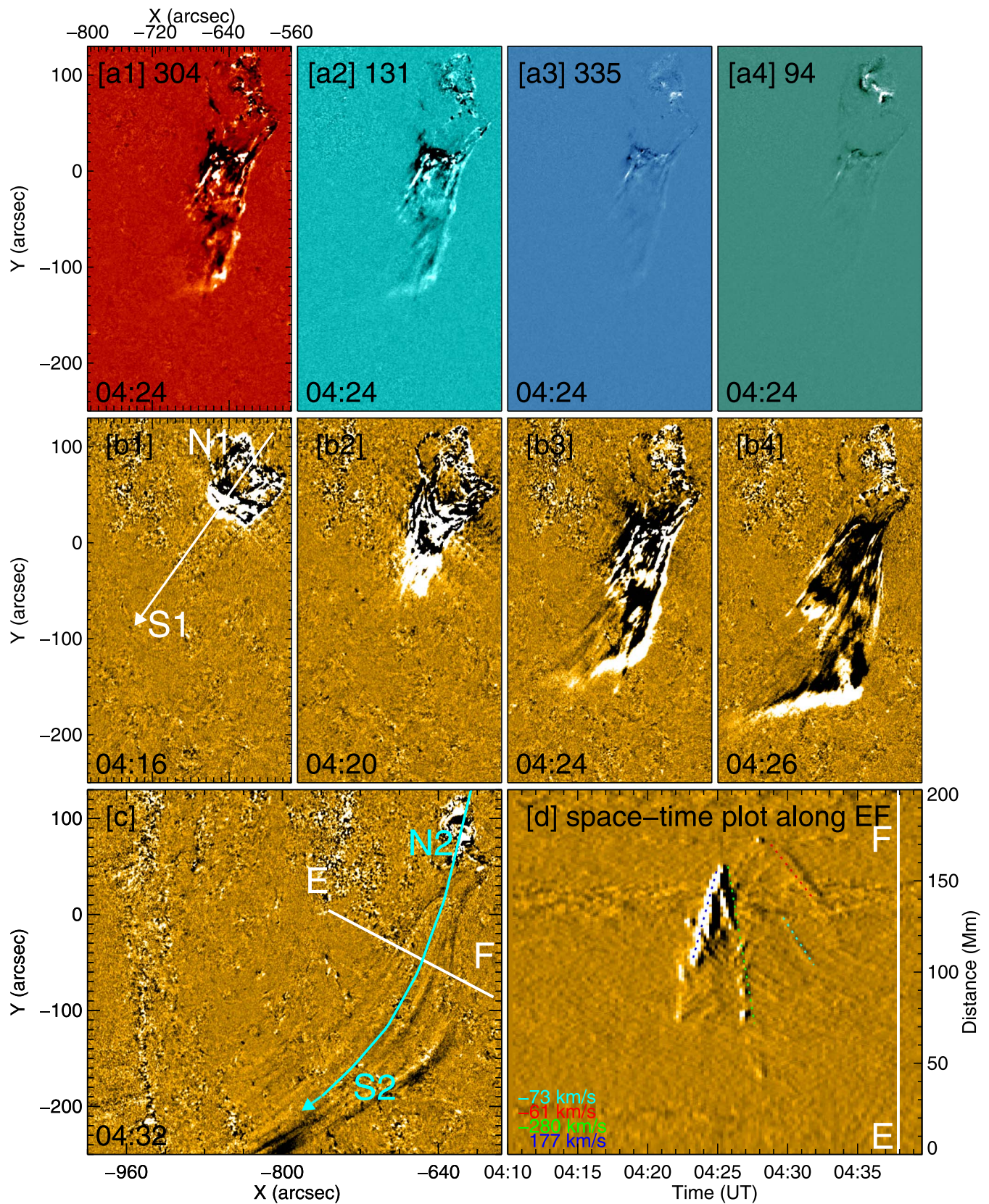


Figure 4. Panels (a1)–(a4): multi-wavelengths observation of the EUV jet. Panels (b1)–(b4): time sequence of AIA 171 Å running-difference images demonstrate the eruption of the jet. In panels (b1) and (c), the white arrow N1–S1 and the cyan arrow N2–S2 mark the slit position of the time–distance plot shown in Figures 7(c1)–(c2) and (d1)–(d2), respectively. The time–distance plot along the white line E–F in panel (c) is shown in panel (d), which shows the expansion and contraction of the remote open coronal loops. The expansion and contraction motions of the loops are marked by four dashed lines in panel (d) with different colors. An animation of panel (c) is available. The animation covers 04:08–04:33 UT with a 12 s cadence. The animation duration is 5 s.

(An animation of this figure is available.)

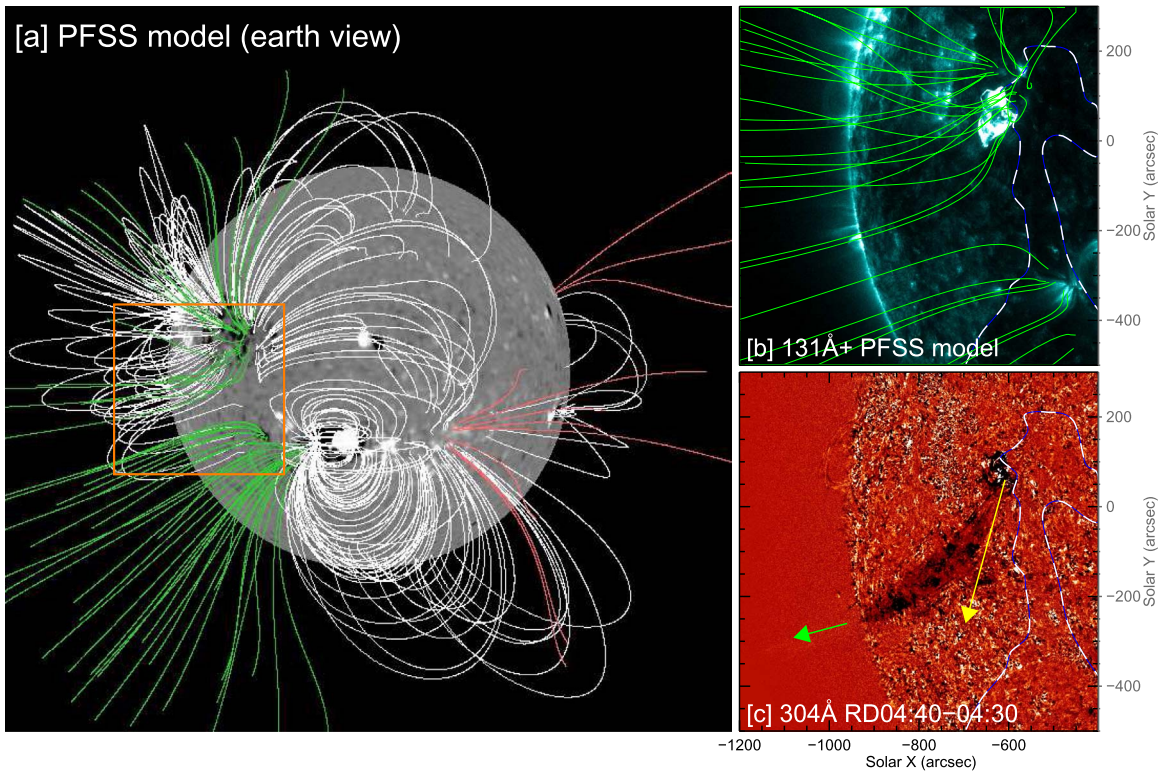


Figure 5. Panel (a): HMI full-disk magnetogram overlaid with the extrapolated magnetic field lines, in which the green and red lines show that the open field lines originated from the negative and positive polarities, respectively. The brown box in panel (a) shows the FOV of panels (b) and (c). Panel (b): AIA 131 Å images overlaid with the remote open field lines (green). Panel (c): AIA 304 Å running-difference image, in which the yellow and green arrows indicate the eruption directions of the jet before and after the interaction with the remote open field lines. The white-blue dashed outlines the nearby coronal hole in panels (b) and (c).

synoptic magnetic maps from HMI with a 6 hr cadence. Some representative global field lines are shown in panel (a), in which the green and white lines are open and closed magnetic field lines, respectively. For a better comparison, the AIA 131 Å and 304 Å running-difference images of the brown box region shown in panel (a) are plotted in panels (b) and (c), respectively. The open field lines rooted in the eruption source region and the remote open field lines in the southern hemisphere are overlaid in the AIA 131 Å image, while the ejection directions of the blowout jet are indicated by the yellow and green arrows in the AIA 304 Å running-difference image. It is clear that the change of the ejection direction of the blowout jet was caused by the blockage of another group of open field lines rooted in the southern hemisphere, supporting the scenario that an open magnetic flux can act as a potential wall so that solar eruptions cannot penetrate it and have to be deflected away (Gopalswamy et al. 2009; Kilpua et al. 2009; Yang et al. 2018).

Intriguingly, following the ejection of the blowout jet toward the outer corona, a twin CME (one was of a jetlike shape and the other was of a bubble-like shape) were captured by the *SOHO*/LASCO (see Figure 6 and its animation). The jetlike CME was ahead of the bubble-like one. The first appearance of the jetlike CME was identified at 04:36 UT in the field of view (FOV) of LASCO/C2 (indicated by the black arrow in panel (b)), while that for the bubble-like CME was at 05:00 UT (indicated by the white arrow in panel (c2)). By comparing the initial eruption direction of the blowout jet in the inner corona (see panel (a)) and the jetlike CME in the outer corona (see panel (c1)), one can find that their eruption directions showed a

large difference. As discussed in the above, the blowout jet was deflected by a group of remote open field lines in the southern hemisphere. The eastward jetlike CME suggests that the angle between the injection and reflection directions of the blowout jet was about 90° . The jetlike CME showed a collimated and elongated structure with an angular width of about $\lesssim 15^\circ$, resembling many typical jetlike CMEs reported in previous studies (Wang et al. 1998; Wang & Sheeley 2002; Vourlidas et al. 2013). The bubble-like CME appeared 24 minutes later than the jetlike one in the FOV of LASCO/C2, and it has an angular width of about 48° . The kinematic evolution of the jetlike CME and the bubble-like CME in LASCO are plotted in panel (d). By fitting the data points with linear and second order functions, we find that the projection speed and deceleration of the jetlike CME were about 895 km s^{-1} and 36 m s^{-2} , respectively. The bubble-like CME can only be identified in the FOV of LASCO/C2 in four successful images; a linear fit to these data points finds that the projection speed of the bubble-like CME was about 340 km s^{-1} . Assuming the CMEs propagated with the obtained average speeds before they reached up to the FOV of LASCO/C2, we can extrapolate their onset times back to one solar radius when they were on the solar surface. As shown in panel (d), the onset time of the eruption of the bubble-like CME is found to be around 04:12 UT (denoted by the red arrow); while that of the jetlike CME is around 04:19 UT (denoted by the blue arrow). The extrapolated onset times of the jetlike and bubble-like CMEs are in good agreement with the start times of the filament eruption and the generation of the blowout jet.

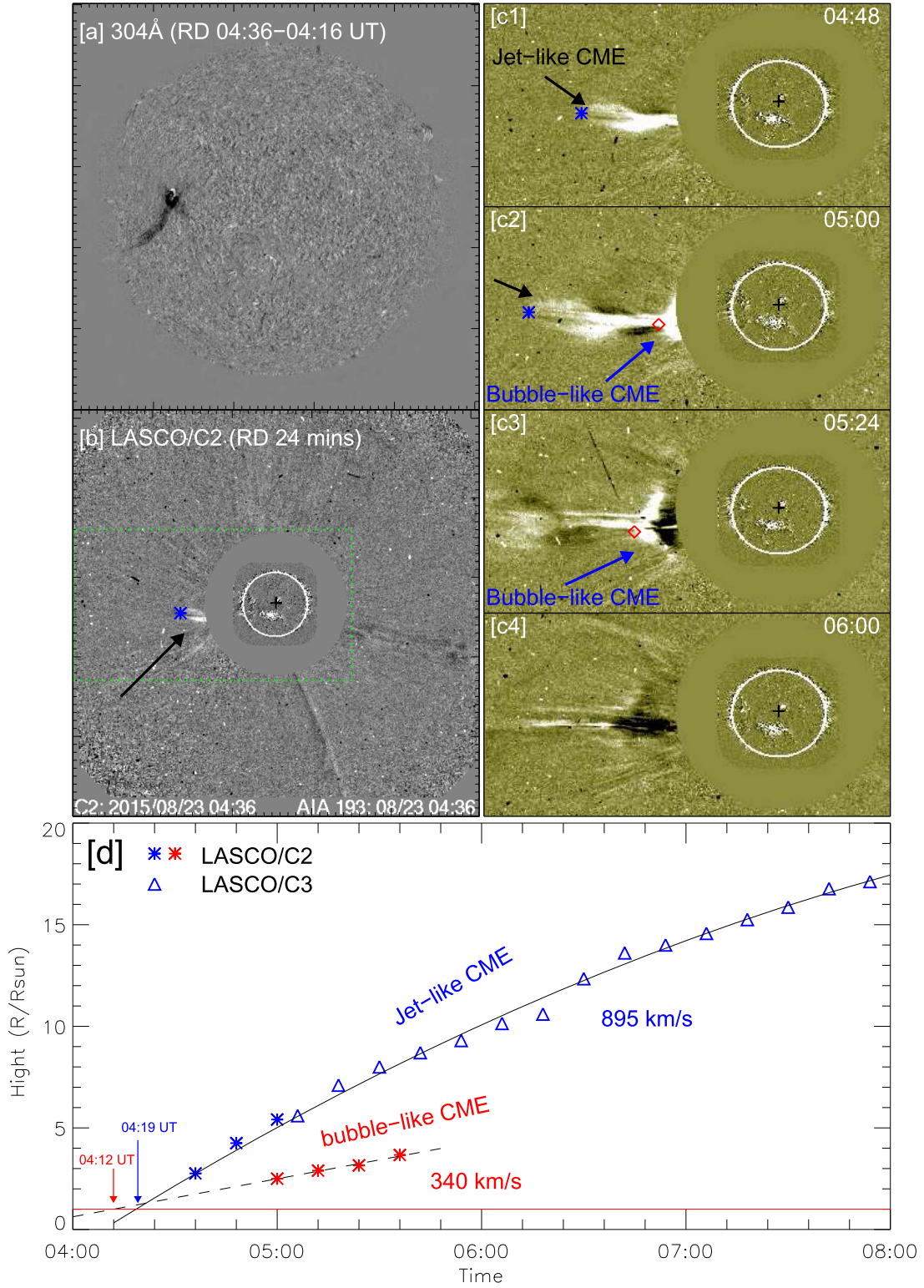


Figure 6. Panels (a) and (b): the running-difference images of AIA 304 Å and LASCO/C2 images display the jet in inner and outer corona, respectively. The green dashed box denote the FOV of panels (c1)–(c4) that show the evolution of the twin CME. In panels (c1)–(c4), the blue asterisk and red diamond mark the front of the jetlike CME and bubble-like CME, respectively; the white circle and the black cross indicate the disk limb and the center of the Sun, respectively. Panel (d): the kinematics of the jetlike CME and the bubble-like CME, in which the red line marks one solar radius. An animation of panel (b) is available. The animation covers 03:12–07:24 UT with a 12-minute cadence.

(An animation of this figure is available.)

The kinematic evolution of the eruptive mini-filament/blowout jet, the light curves in the eruption source region, and the associated type-III radio burst are shown in Figure 7. The

kinematics of the mini-filament and the jet are shown in panels (c1)–(c2) and (d1)–(d2), respectively. Based on these time-distance diagrams, the speed of the mini-filament is found to be

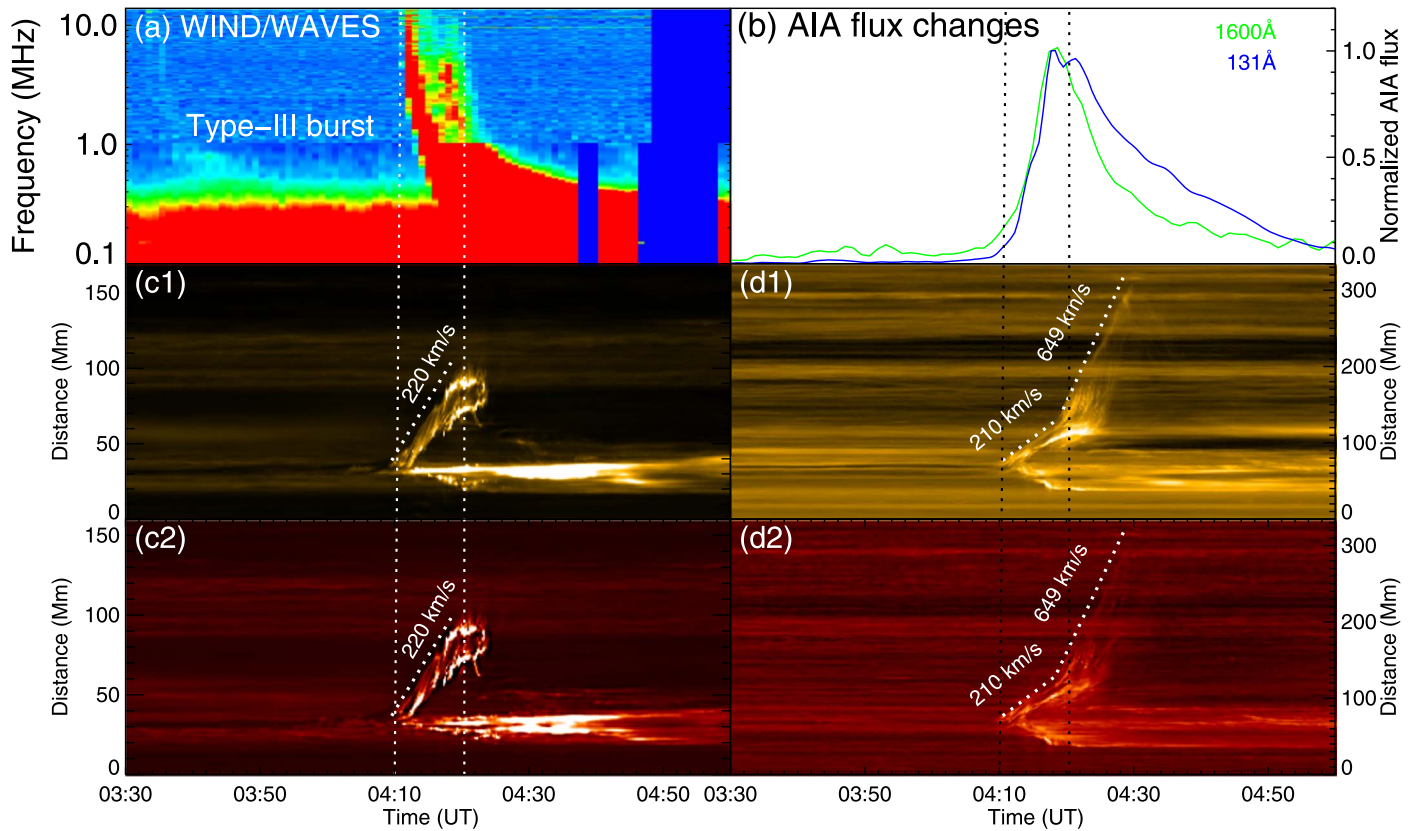


Figure 7. Panel (a): radio dynamic spectra obtained by RAD1 and RAD2 on board *Wind*/WAVES. Panel (b): AIA 1600 Å (green) and 131 Å (blue) light curves within the eruptive source region as outlined by the cyan dashed box in Figure 2(e). Panels (c1)–(c2): the time–distance plot along the line N1–S1 in Figure 4(b1). Panels (d1)–(d2): the time–distance plot along the line N2–S2 in Figure 4(c). The dotted black lines indicate the time 04:10 UT and 04:20 UT, respectively.

about 220 km s^{-1} , while that for the jet is about 649 km s^{-1} . As shown in panel (b), the associated flare’s start, peak, and end times were about 04:10 UT, 04:20 UT, and 04:30 UT, respectively. Moderate flux increase can be identified in the AIA 1600 and 131 Å light curves during the slow rising phase of the mini-filament (before 04:10 UT); then, the violent eruption phase of the mini-filament corresponded the impulsive phase of the light curves. During this stage, the mini-filament erupted with the velocity of about $210\text{--}220 \text{ km s}^{-1}$. During the flare decay phase (after 04:20 UT), the jet is seen to have been accelerated to a speed of about 649 km s^{-1} . In addition, an obvious type-III radio burst was detected by the *Wind*/WAVES (see panel (a)), which rapidly drifted from about 10 MHz to a very low frequency ($\sim 0.1\text{--}0.3 \text{ MHz}$). Based on the leading radio burst theory, the appearance of type-III radio burst means that a population of near-relativistic electrons stream from the eruptive source region to interplanetary space along open magnetic field lines (Reid & Ratcliffe 2014; Shen et al. 2017). Therefore, the type-III radio burst observed here evidenced the reconnection process between the rising filament and the ambient open field lines.

4. Summary and Discussion

In this paper, we present a direct imaging observation of a twin CME that evolved from a coronal blowout jet, which involved the eruption of a mini-filament in the jet’s eruption source region. The generation of the blowout jet was due to the magnetic reconnection between the rising filament and the ambient open coronal loops. It is interesting that the ejection of

the blowout jet experienced an obvious deflection of about 90° due to the blockage of a group of remote open coronal field lines in the southern hemisphere. The deflection significantly changed the ejection direction of the blowout jet from southward to almost eastward. Analysis results of the photospheric magnetic fields suggest that the activation and slow rise of the mini-filament was associated with the magnetic flux cancellation in the filament channel, while the sudden emergence of the positive magnetic flux was possibly responsible for the violent fast eruption of the filament. Moreover, quasi-periodic intermittent jetlike activities are also observed in the filament channel in the course of flux cancellation, which may also play a role in the filament eruption (see also Tian et al. 2018b). Compared to previous studies, the present event suffered less projection effect, and it can provide more accurate information for mini-filament-driven blowout jets, as well as the twin CME.

CMEs have been studied for many years, and various models are proposed to interpret their formation, evolution, and propagation mechanisms (Chen 2011). The most previous observations indicated that a single solar eruption in the inner corona always results in a corresponding large-scale CME. Only a small fraction of solar eruptions can launch multiple CMEs in different ways. For example, Jiang et al. (2008) reported that a sympathetic CME pair was physically connected to an on-disk jet, in which one was related to the flare and jet, while the other was due to the eruption of an interconnecting loop caused by the interaction of the jet plasma. Shen et al. (2012a) reported the sympathetic filament eruptions in a breakout magnetic configuration; they found that the two

adjacent filaments erupted sequentially and proposed that there would be two corresponding CMEs in the outer corona within the framework of the magnetic breakout model. Global EUV waves can propagate to large distances and can trigger multiple solar eruptions in their path (Shen et al. 2014a, 2014b); therefore, they could potentially result in the possible occurrence of multiple solar eruptions and CMEs within a short time interval.

Nevertheless, so far, reports on the simultaneous appearance of a pair of CMEs evolved from one single jet are still very scarce in the literature. The first report on such kind of an eruption was published by Shen et al. (2012b), where they found a typical filament-driven blowout jet that showed cool dark and hot bright components in the inner corona, whereas in the outer corona, they detected a pair of simultaneous CMEs, i.e., a jetlike CME and a bubble-like CME. Those authors also proposed a model to interpret this interesting eruption, in which the jetlike CME first resulted from the hot bright jet component that was produced by a preceding external reconnection between the rising confining fields of the mini-filament and the ambient open field lines, while the bubble-like one subsequently developed from the ensuing eruption of the mini-filament due to the removal of the confining field of the mini-filament by the external reconnection.

In the present case, a similar twin CME was also observed by LASCO after the mini-filament eruption. Combining the STEREO-A EUVI and SDO/AIA observations, we found that no other obvious eruptions occurred from 03:30 UT to 05:00 UT, which allowed us to exclude the backside eruptions. In order to relate the twin CME back into their solar counterparts, we further investigate the kinematics of the jetlike and the bubble-like CMEs, respectively. The height–time relationship of the twin CME have been presented in Figure 6(d), in which one can clearly see that the jetlike one first appeared in the FOV of LASCO/C2 at around 04:36 UT and finally propagated to a 17 solar radius at an averaged speed of around 895 km s^{-1} , while the bubble-like CME had only been captured by LASCO/C2 during 05:00–05:36 UT, which had a speed of about 340 km s^{-1} and faded away within a 5 solar radius. The extrapolated onset times of the bubble-like and the jetlike CMEs are about 04:12 UT and 04:19 UT, respectively. Based on the close temporal and spatial relationship between the twin CME and their solar counterparts, we conclude that the bubble-like CME should correspond to the eruption of the mini-filament that started at around 04:10 UT with the a speed of about $210\text{--}220 \text{ km s}^{-1}$, while the jetlike CME should be the coronal extension of the blowout jet that began at about 04:20 UT with a speed of about 649 km s^{-1} . It is worth noting that in our event, the loss of equilibrium of the mini-filament happened at first, while the external reconnection should be triggered due to the interaction between the rising filament and the background open field, which is different from the event reported by Shen et al. (2012b). Although we did not detect this bright hot jet component during the eruption in the inner corona (see the Figures 4(a1)–(a4)), the detected type-III radio burst and the rearrangement of the coronal loops do indicate the occurrence of the reconnection.

Our analysis results indicate that the start time of the jetlike CME was after the bubble-like one for a few minutes; however, the former was captured by LASCO earlier than the later, which implies that the jetlike CME underwent a more prominent acceleration after its initiation. The ejecting speed

of the jetlike CME was about 895 km s^{-1} ; such a high speed was possibly due to the following reasons. We note that the jet experienced an interaction process with a group of remote open field lines that caused the deflection of the ejecting direction of the jet plasma. During the interaction process, we do not find any signatures of energy dissipation at the interaction site. The significant acceleration of the jet plasma may be mainly due to the acceleration of the slingshot effect of the bended open loops caused by the interaction. The untwisting motion of the jet represents the releasing of non-potential magnetic energy stored in the pre-eruption filament, which can also contribute to the acceleration of the jet (Shen et al. 2011b). In addition, we argue that during the interaction period, a part of the jet plasma may stay at the interaction site or fall back to the solar surface; therefore, only a portion of the initial ejecting plasma was accelerate to the outer corona. In that case, the total kinetic energy of the initial jet plasma was transformed into the kinetic energy of the portion of the ejected plasma after the interaction. Due to the decreased mass, the ejecting portion of the jet plasma can also obtain a higher speed. Regarding bubble-like CME, its speed was about 340 km s^{-1} . Such a speed indicates that the bubble-like CME should be a slow CME that is often associated with filament eruption (Gosling et al. 1976). In the present event, the bubble-like CME did associated with the eruption of a mini-filament, which could possibly account for its relatively lower ejecting speed.

Many observations have revealed that solar eruptions can be channeled and guided by neighboring large-scale background magnetic fields during their initial stage. When erupting magnetized plasma interact with remote magnetic structures, they are often deflected to the direction of minimum magnetic force on global scales (Nisticò et al. 2015). In the highly complicated corona, there are many magnetic structures (i.e., active regions, coronal holes, and helmet streamers) can act as obstacles and impose actions on solar eruptions impeding on them. Previous studies suggested that erupting filaments may tend to propagate to the region with the weak field or lower magnetic energy density (Bi et al. 2011; Shen et al. 2011a) and that CMEs can be channeled and guided by large-scale magnetic fields, such as streamers and open fields in coronal holes (Filippov et al. 2001; Plunkett et al. 2001; Bemporad et al. 2005; Jiang et al. 2007; Bi et al. 2013; Zheng et al. 2016; Yang et al. 2018). For the interaction between CMEs and open field lines, such as in coronal holes, Gopalswamy et al. (2009) proposed two possible consequences for the interaction depending on their relative directions of the field lines. When the magnetic fields of the CME are parallel to the open field lines, the CME will be deflected due to its lower horizontal speed component relative to the Alfvén speed in the coronal hole. When the magnetic field lines are antiparallel to each other, magnetic reconnection can be expected between them. Aided by the PFSS model, we identified that the deflection of the blowout jet or CME in the present study was due to the blockage of a group of remote open field lines rooted in the southern hemisphere. The extrapolated coronal field lines reveals that the magnetic field of the blowout jet and the remote open field lines in the southern hemisphere were parallel; therefore, there should be no reconnection between them. In addition, the extrapolated coronal magnetic field also revealed that the eruption direction of the CMEs were consistent with that of the bent open field lines. Therefore, these field lines also channeled the propagation of the CMEs.

The authors would like to thank the data provided by the *SDO*, *SOHO*/LASCO, and *Wind* science teams; the anonymous referee's valuable comments and suggestions that largely improved the quality of the paper; and the helpful discussions with Dr. Yu Liu and Junchao Hong from Yunnan Observatories, CAS, China. This work is supported by the Natural Science Foundation of China (11773068, 1163308, and 11363007), the Yunnan Science Foundation (2017FB006), and the West Light Foundation of Chinese Academy of Sciences. H.C.C. acknowledges the support by NSFC 11703084, 11633008, and 11873088.

ORCID iDs

Yuandeng Shen  <https://orcid.org/0000-0001-9493-4418>

Hechao Chen  <https://orcid.org/0000-0001-7866-4358>

References

- Adams, M., Sterling, A. C., Moore, R. L., & Gary, G. A. 2014, *ApJ*, **783**, 11
- Alzate, N., & Morgan, H. 2016, *ApJ*, **823**, 129
- Archontis, V., & Hood, A. W. 2013, *ApJL*, **769**, L21
- Bemporad, A., Sterling, A. C., Moore, R. L., & Poletto, G. 2005, *ApJL*, **635**, L18
- Bi, Y., Jiang, Y., Yang, J., et al. 2013, *ApJ*, **773**, 162
- Bi, Y., Jiang, Y. C., Yang, L. H., & Zheng, R. S. 2011, *NewA*, **16**, 276
- Bougeret, J.-L., Kaiser, M. L., Kellogg, P. J., et al. 1995, *SSRv*, **71**, 231
- Brueckner, G. E., Howard, R. A., Koomen, M. J., et al. 1995, *SoPh*, **162**, 357
- Byrne, J. P., Maloney, S. A., McAteer, R. T. J., Refojo, J. M., & Gallagher, P. T. 2010, *NatCo*, **1**, 74
- Canfield, R. C., Reardon, K. P., Leka, K. D., et al. 1996, *ApJ*, **464**, 1016
- Chae, J., Qiu, J., Wang, H., & Goode, P. R. 1999, *ApJL*, **513**, L75
- Chen, H., Zhang, J., Cheng, X., et al. 2014, *ApJL*, **797**, L15
- Chen, H., Zhang, J., Ma, S., Yan, X., & Xue, J. 2017, *ApJL*, **841**, L13
- Chen, H.-D., Zhang, J., & Ma, S.-L. 2012, *RAA*, **12**, 573
- Chen, P. F. 2011, *LRSF*, **8**, 1
- Davies, J. A., Perry, C. H., Trines, R. M. G. M., et al. 2013, *ApJ*, **777**, 167
- Feng, L., Inhester, B., de Patoul, J., Wiegmann, T., & Gan, W. Q. 2012, *A&A*, **538**, A34
- Filippov, B. P., & Den, O. E. 2018, *ARep*, **62**, 359
- Filippov, B. P., Gopalswamy, N., & Lozhechkin, A. V. 2001, *SoPh*, **203**, 119
- Gopalswamy, N., Mäkelä, P., Xie, H., Akiyama, S., & Yashiro, S. 2009, *JGRA*, **114**, A00A22
- Gopalswamy, N., Yashiro, S., Krucker, S., Stenborg, G., & Howard, R. A. 2004, *JGRA*, **109**, A12105
- Gosling, J. T., Hildner, E., MacQueen, R. M., et al. 1976, *SoPh*, **48**, 389
- Gui, B., Shen, C., Wang, Y., et al. 2011, *SoPh*, **271**, 111
- Harvey, J. W., Bolding, J., Clark, R., et al. 2011, *BAAS*, **43**, 17
- Hong, J., Jiang, Y., Yang, J., et al. 2016, *ApJ*, **830**, 60
- Hong, J., Jiang, Y., Yang, J., Li, H., & Xu, Z. 2017, *ApJ*, **835**, 35
- Hong, J.-C., Jiang, Y.-C., Yang, J.-Y., et al. 2013, *RAA*, **13**, 253
- Hou, Y., Li, T., Yang, S., & Zhang, J. 2019, *ApJ*, **871**, 4
- Howard, R. A., Moses, J. D., Vourlidas, A., et al. 2008, *SSRv*, **136**, 67
- Huang, Z., Mou, C., Fu, H., et al. 2018, *ApJL*, **853**, L26
- Isavnin, A., Vourlidas, A., & Kilpua, E. K. J. 2013, *SoPh*, **284**, 203
- Jiang, Y., Bi, Y., Yang, J., et al. 2013, *ApJ*, **775**, 132
- Jiang, Y., Shen, Y., Yi, B., Yang, J., & Wang, J. 2008, *ApJ*, **677**, 699
- Jiang, Y., Yang, L., Li, K., & Shen, Y. 2007, *ApJL*, **667**, L105
- Joshi, R., Schmieder, B., Chandra, R., et al. 2017, *SoPh*, **292**, 152
- Kaiser, M. L., Kucera, T. A., Davila, J. M., et al. 2008, *SSRv*, **136**, 5
- Kay, C., Opher, M., & Evans, R. M. 2013, *ApJ*, **775**, 5
- Kilpua, E. K. J., Pomoell, J., Vourlidas, A., et al. 2009, *AnGeo*, **27**, 4491
- Kundu, M. R., Raulin, J.-P., Nitta, N., Shibata, K., & Shimojo, M. 1998, *SoPh*, **178**, 173
- Lee, E. J., Archontis, V., & Hood, A. W. 2015, *ApJL*, **798**, L10
- Lemen, J. R., Title, A. M., Akin, D. J., et al. 2012, *SoPh*, **275**, 17
- Li, H., Jiang, Y., Yang, J., et al. 2017a, *ApJ*, **836**, 235
- Li, H., Jiang, Y., Yang, J., et al. 2017b, *ApJL*, **842**, L20
- Li, H., & Yang, J. 2019, *ApJ*, **872**, 87
- Li, H., Yang, J., Jiang, Y., et al. 2018, *Ap&SS*, **363**, 26
- Li, L., & Zhang, J. 2013, *SoPh*, **282**, 147
- Li, X., Yang, S., Chen, H., Li, T., & Zhang, J. 2015, *ApJL*, **814**, L13
- Li, X., Zhang, J., Yang, S., Hou, Y., & Erdélyi, R. 2018, *NatSR*, **8**, 8136
- Lin, J., & Forbes, T. G. 2000, *JGR*, **105**, 2375
- Liu, R., Liu, C., Wang, S., Deng, N., & Wang, H. 2010a, *ApJL*, **725**, L84
- Liu, W., Berger, T. E., Title, A. M., & Tarbell, T. D. 2009, *ApJL*, **707**, L37
- Liu, Y. 2008, *SoPh*, **249**, 75
- Liu, Y., & Kurokawa, H. 2004, *ApJ*, **610**, 1136
- Liu, Y., Su, J. T., Morimoto, T., Kurokawa, H., & Shibata, K. 2005, *ApJ*, **628**, 1056
- Liu, Y., Themisien, A., Luhmann, J. G., et al. 2010b, *ApJ*, **722**, 1762
- MacQueen, R. M., Hundhausen, A. J., & Conover, C. W. 1986, *JGR*, **91**, 31
- Miao, Y., Liu, Y., Li, H. B., et al. 2018, *ApJ*, **869**, 39
- Miao, Y., Liu, Y., Shen, Y. D., et al. 2019, *ApJ*, **877**, 61
- Moore, R. L., Cirtain, J. W., Sterling, A. C., & Falconer, D. A. 2010, *ApJ*, **720**, 757
- Nisticò, G., Bothmer, V., Patsourakos, S., & Zimbardo, G. 2009, *SoPh*, **259**, 87
- Nisticò, G., Bothmer, V., Patsourakos, S., & Zimbardo, G. 2010, *AnGeo*, **28**, 687
- Nisticò, G., Zimbardo, G., Patsourakos, S., Bothmer, V., & Nakariakov, V. M. 2015, *A&A*, **583**, A127
- Panesar, N. K., Sterling, A. C., Moore, R. L., & Chakrapani, P. 2016, *ApJL*, **832**, L7
- Paraschiv, A. R., Lacatus, D. A., Badescu, T., et al. 2010, *SoPh*, **264**, 365
- Pesnell, W. D., Thompson, B. J., & Chamberlin, P. C. 2012, *SoPh*, **275**, 3
- Plunkett, S. P., Thompson, B. J., St., Cyr, O. C., & Howard, R. A. 2001, *JASTP*, **63**, 389
- Reid, H. A. S., & Ratcliffe, H. 2014, *RAA*, **14**, 773
- Roy, J.-R. 1973, *SoPh*, **32**, 139
- Scherrer, P. H., Schou, J., Bush, R. I., et al. 2012, *SoPh*, **275**, 207
- Schrijver, C. J., & De Rosa, M. L. 2003, *SoPh*, **212**, 165
- Shen, C., Wang, Y., Gui, B., Ye, P., & Wang, S. 2011a, *SoPh*, **269**, 389
- Shen, Y., Chen, P. F., Liu, Y. D., et al. 2019, *ApJ*, **873**, 22
- Shen, Y., Ichimoto, K., Ishii, T. T., et al. 2014a, *ApJ*, **786**, 151
- Shen, Y., Liu, Y., Liu, Y. D., et al. 2018a, *ApJ*, **861**, 105
- Shen, Y., Liu, Y., Song, T., & Tian, Z. 2018b, *ApJ*, **853**, 1
- Shen, Y., Liu, Y., & Su, J. 2012a, *ApJ*, **750**, 12
- Shen, Y., Liu, Y., Su, J., & Deng, Y. 2012b, *ApJ*, **745**, 164
- Shen, Y., Liu, Y., Su, J., & Ibrahim, A. 2011b, *ApJL*, **735**, L43
- Shen, Y., Liu, Y. D., Chen, P. F., & Ichimoto, K. 2014b, *ApJ*, **795**, 130
- Shen, Y., Liu, Y. D., Su, J., Qu, Z., & Tian, Z. 2017, *ApJ*, **851**, 67
- Shen, Y., Tang, Z., Li, H., & Liu, Y. 2018c, *MNRAS*, **480**, L63
- Shen, Y., Tang, Z., Miao, Y., Su, J., & Liu, Y. 2018d, *ApJL*, **860**, L8
- Shen, Y.-D., Liu, Y., & Liu, R. 2011c, *RAA*, **11**, 594
- Shibata, K., Ishido, Y., Acton, L. W., et al. 1992, *PASJ*, **44**, L173
- Shibata, K., Nitta, N., Strong, K. T., et al. 1994, *ApJL*, **431**, L51
- Solanki, R., Srivastava, A. K., Rao, Y. K., & Dwivedi, B. N. 2019, *SoPh*, **294**, 68
- Sterling, A. C., Harra, L. K., Moore, R. L., & Falconer, D. A. 2019, *ApJ*, **871**, 220
- Sterling, A. C., Moore, R. L., Falconer, D. A., et al. 2016, *ApJ*, **821**, 100
- Sterling, A. C., Moore, R. L., Falconer, D. A., & Adams, M. 2015, *Natur*, **523**, 437
- Tian, H., DeLuca, E. E., Cranmer, S. R., et al. 2014, *Sci*, **346**, 1255711
- Tian, H., Zhu, X., Peter, H., et al. 2018a, *ApJ*, **854**, 174
- Tian, Z., Liu, Y., Shen, Y., et al. 2017, *ApJ*, **845**, 94
- Tian, Z., Shen, Y., & Liu, Y. 2018b, *NewA*, **65**, 7
- Vourlidas, A., Lynch, B. J., Howard, R. A., & Li, Y. 2013, *SoPh*, **284**, 179
- Wang, Y.-M., & Sheeley, N. R., Jr. 2002, *ApJ*, **575**, 542
- Wang, Y.-M., Sheeley, N. R., Jr., Socker, D. G., et al. 1998, *ApJ*, **508**, 899
- Wuelser, J.-P., Lemen, J. R., Tarbell, T. D., et al. 2004, *Proc. SPIE*, **5171**, 111
- Yang, B., & Chen, H. 2019, *ApJ*, **874**, 96
- Yang, J., Dai, J., Chen, H., Li, H., & Jiang, Y. 2018, *ApJ*, **862**, 86
- Yang, J., Jiang, Y., Yang, B., et al. 2012a, *NewA*, **17**, 732
- Yang, J.-Y., Jiang, Y.-C., Yang, D., et al. 2012b, *RAA*, **12**, 300
- Yang, L.-H., Jiang, Y.-C., Yang, J.-Y., et al. 2011, *RAA*, **11**, 1229
- Yang, S., & Zhang, J. 2018, *ApJL*, **860**, L25
- Yashiro, S., Gopalswamy, N., Cliver, E. W., et al. 2004, in ASP Conf. Ser. 325, *The Solar-B Mission and the Forefront of Solar Physics*, ed. T. Sakurai & T. Sekii (San Francisco, CA: ASP), 401
- Yokoyama, T., & Shibata, K. 1995, *Natur*, **375**, 42
- Yokoyama, T., & Shibata, K. 1996, *PASJ*, **48**, 353
- Zhang, J., Wang, J., & Liu, Y. 2000, *A&A*, **361**, 759
- Zhang, Q. M., & Ji, H. S. 2014, *A&A*, **567**, A11
- Zhang, Y., & Zhang, J. 2017, *ApJ*, **834**, 79
- Zheng, R., Chen, Y., Du, G., & Li, C. 2016, *ApJL*, **819**, L18
- Zheng, R., Chen, Y., Huang, Z., et al. 2018, *ApJ*, **861**, 108
- Zhou, Y. F., & Feng, X. S. 2013, *JGRA*, **118**, 6007
- Zhu, X., Wang, H., Cheng, X., & Huang, C. 2017, *ApJL*, **844**, L20